In situ characterization of one-dimensional plasmonic Ag nanocluster arrays

R. Verre,* K. Fleischer, R. G. S. Sofin, N. McAlinden, J. F. McGilp, and I. V. Shvets
Centre for Research on Adaptive Nanostructures and Nanodevices (CRANN), School of Physics, Dublin 2, Ireland
(Received 1 September 2010; revised manuscript received 10 January 2011; published 30 March 2011)

One-dimensional Ag nanoparticle arrays have been grown on step-bunched vicinal Al_2O_3 in ultrahigh vacuum using deposition at a glancing angle. The structures grown showed a strong optical anisotropy in the visible region of the spectrum. The optical anisotropy was measured *in situ* using reflection anisotropy spectroscopy. Relevant optical properties were determined as a function of deposition angle and Ag thickness. A simple phenomenological model was developed to reproduce the features seen in the spectra. With this model it was possible to use the inhomogeneous broadening as a guide to the nanoparticle dispersion.

DOI: 10.1103/PhysRevB.83.125432 PACS number(s): 61.46.−w, 78.67.−n, 81.07.−b

I. INTRODUCTION

Localized plasmon resonances (LPRs) are collective excitations of the free electron gas in metal nanoparticles (NPs) excited by an incident electromagnetic wave. The main manifestation of the interaction process is a peaked absorption band in the UV-visible range.[1,2] This, together with a high surface-to-volume ratio, makes LPR promising for many nanophotonics[3,4] and biochemistry applications.[5,6] One of the key aspects of LPR is the possibility of tuning the spectral peak position by changing the shape, the dimension of the NP, or the dielectric medium of the environment surrounding the NP. In particular, advances in nanostructure preparation, especially via colloidal chemistry,[7,8] provide an easy and inexpensive way for changing the NP morphology and related optical properties. Most prototype devices, on the other hand, involve the deposition of NP from suspension onto substrates. However, using this method, one cannot easily produce systems with long-range order. Lithographic techniques could potentially offer a solution, but their low output and high production costs make them inappropriate for most practical purposes. The development of a glancing-angle deposition method on nanostructured grooved templates represents a possible solution, where long-range order and a fast output can be combined. This approach has already been exploited to produce a variety of systems, both on single-crystalline surfaces[9–11] and on amorphous dielectric substrates patterned via ion sputtering.[12,13] In particular, the possibility of growing ordered arrays of Ag nanodots in ultrahigh vacuum (UHV) possessing polarization-dependent absorption spectra has been shown.[14–17] Such optical behavior has been commonly observed in numerous mesoscopic structures and is attributed to the coupling of low-dimensional metallic structures.[18–20]

The Ag structures reported by glancing-angle deposition possess dimensions below the resolution of lithographic techniques, survive to atmospheric exposure, and their plasmonic signature is strongly dependent on anisotropic interparticle interactions, making them a peculiar and appealing system to be further characterized.

Reflectance anisotropy spectroscopy (RAS) measures the difference in reflection of light, at normal incidence, polarized in two orthogonal directions divided by the average reflectance,

$$\frac{\Delta r}{r} = 2\frac{r_x - r_y}{r_x + r_y}, \tag{1}$$

where r_i are the complex Fresnel reflection coefficients along the x and y direction, respectively.[21] A detailed review of the experiment and theory of RAS has been published recently.[22] The advantages of RAS are that it provides surface sensitivity, where the substrate is optically isotropic and the surface is anisotropic, and it is possible to use it for monitoring directly in UHV and other environments.[21] RAS has been proved to be a useful tool for the characterization of both semiconductor[23,24] and metallic surfaces.[25,26] Where glancing-angle deposition is used to create anisotropic plasmonic structures, RAS can also be used, in principle, to determine their plasmonic properties *in situ* during growth.

The main limitation of glancing-angle deposition for any practical application is the difficulty in obtaining monodispersed distribution of the NP's morphology during the self-assembled phenomenon. This is reflected in the inhomogeneous broadening of the resonances then causing a loss in sensitivity during measurements of changes of the refractive index of the medium surrounding the particles. The process could be used for optimized tuning of the growth parameters, and this can be reflected in a narrowing of the resonance peaks.

This paper discusses the growth of Ag NP on stepped single-crystal c-plane sapphire surfaces at glancing angles of deposition. The optical characterization has been performed via *in situ* RAS. The possibility of not only measuring the peak resonances during growth but also probing the NP dispersion is demonstrated.

II. EXPERIMENTAL PROCEDURE

Annealed single-crystal c-plane sapphire samples [α-Al_2O_3 (0001)], miscut along the [$1\bar{2}10$] direction, were used to obtain stepped templates. The substrates (MTI Corporation, USA) were prepared with 3° and 6° nominal miscuts. Single-side polished samples were used in all the experiments, and quality and miscut was verified with x-ray diffraction. Each sample was cleaned with HCl, rinsed in deionized water, and then sonicated in an ultrasonic bath with methanol, acetone, and isopropanol. After the solvent treatment the substrates were loaded in a high-purity alumina crucible and put in an alumina tube furnace. The samples were annealed in atmosphere at temperatures above 1000°C for 24 h in order to obtain an ordered terrace and stepped structure. The surface was then scanned with an Asylum Research atomic force microscope

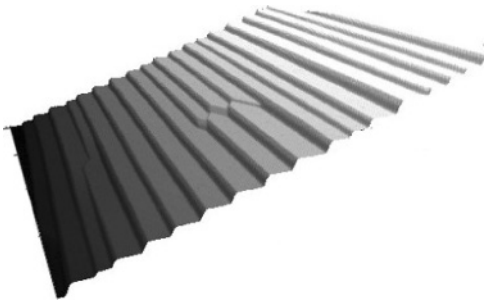

FIG. 1. A 2×2 μm^2 AFM image of a step-bunched *c*-plane Al_2O_3 substrate after first-order subtraction. The surface is off-cut 3° along the $[1\bar{2}10]$ direction. After annealing in atmosphere at 1350 °C for 24 h, the surface is covered by uniform, parallel, and straight steps. The average terrace width and step height are 117 ± 24 and 5.8 ± 1.9 nm, respectively. The substrates have been used for the growth of Ag NP chains deposited at glancing angles. Adatoms would be deposited on the left.

(AFM) in tapping mode to confirm that there was a well-ordered surface (Fig. 1).

The annealed templates were subsequently loaded into the growth chamber (base pressure 3×10^{-8} mbar) and the average sample surface aligned at a required grazing angle with respect to the Ag atom flux. The alignment of each sample was measured by the deflection of a reflected laser spot pointing toward the sample surface. The accuracy of the alignment was $\pm 0.1°$. The NPs were prepared by evaporating Ag onto the substrates at room temperature with a controlled rate at normal incidence of 0.23 nm/min and the RAS spectra were recorded *in situ*. The RAS spectrometer used is home built and follows the Aspnes design.[21] Light from a Xe lamp passes through a polarizer and a low-strain window and is reflected from the sample through a photoelastic modulator, an analyzer polarizer, and a monochromator before finally reaching a double-diode detector system. Measurements were performed over a broad spectral range, from 0.74 to 4 eV. In this work we report results of the real part of the RAS signal only.[22] Index x in Eq. (1) represents the direction along the steps $[10\bar{1}0]$ and y the direction perpendicular to them, along $[1\bar{2}10]$.

Ex situ characterization was performed with a Cary 50 UV-visible (UV-vis) near-infrared (NIR) spectrophotometer equipped with a Xe lamp, and the morphology of the cluster layer was determined using an ULTRA scanning electron microscope (SEM) built by Carl Zeiss.

III. RESULTS

A. Al_2O_3 step bunching and its RAS signature

The first report of step bunching of α-Al_2O_3 (0001) dates back to more than a decade ago, when single crystals were annealed in air at high temperatures.[27] Prior to annealing, the polished surface was covered with monoatomic steps oriented along the $[10\bar{1}0]$ direction and with a height of 0.22 nm.[28] After heating to temperatures above 1000 °C, a gathering of the steps was observed, leading to steps as high as ~1.2 nm.

More recently, reports have shown a similar behavior for vicinal samples,[29] producing step-bunched surfaces with a smaller terrace width and higher step. The annealing experiments have been reproduced and the typical result is shown in Fig. 1. After heating to temperatures above 1200 °C, the *c*-plane alumina surfaces consist of wide terraces separated by aligned straight steps, with a typical length of more than 5 μm. The mechanism behind the step-bunching phenomenon of Al_2O_3 and dependency of the step height and terrace width upon changes in miscut angle and annealing temperature is beyond the scope of this paper. The step height and terrace width can be tuned by changing the annealing conditions and vicinal angle.

The choice of *c*-plane α-alumina as a template for the growth of Ag NPs has been motivated by symmetry considerations. Until now the only RAS measurement of dipolar excitations of Ag NP have been performed by Flores-Camacho *et al.* on *m*-plane sapphire.[30] In their report it was shown that the anisotropic substrate creates anisotropic image charges that can produce a RAS signal. Flat *c*-plane Al_2O_3 possesses a threefold symmetry that should not give rise to any distinct signature in the RAS spectrum.[22] Despite that, the presence of the miscut could in theory introduce anisotropic contributions that could modify the optical properties of the Ag assembly. In order to eliminate this possibility, the RAS spectra of the clean vicinal substrates were recorded. They consisted of a small signal in the UV of 2×10^{-3}, confirming that the substrate signature in the measured spectral range was negligible with respect to the signal obtained after Ag deposition (for comparison, see Fig. 3).

B. Transmission and RAS comparison

To understand the origin of the RAS signature, we first demonstrate the equivalence between RAS and polarized transmission spectroscopy (PTS) for the system investigated. For this, a test sample with a 3° miscut angle was annealed at 1400 °C. AFM confirmed a surface morphology similar to the sample shown in Fig. 1. Subsequently, the substrate was loaded into the chamber and aligned at 6° with respect to the collimated beam of evaporant metal using a precision manipulator. Ag was deposited for 20 min for an NP height $h = 4$ nm. The NP height was estimated as $h = F \times t \times \sin\Theta / f$, where F is the adatom rate flux at normal incidence, t is the deposition time, Θ is the grazing deposition angle, and the nanocluster filling factor, $f \simeq 0.12$. After exposure of the sample to atmosphere, both RAS and PTS were measured and the results were compared qualitatively in Fig. 2(a). PTS shows a distinct peak and its resonant position depends on the polarization angle of the incident light. When the beam is polarized along the miscut direction, the absorption spectrum contains a main peak in the UV, while if the beam is polarized along the step edge, the main peak resonance is present at lower energy and has a higher intensity. This is in accordance with previous literature reports.[15–17,31] Similarly, the RAS spectrum presents a double resonance whose positions match the absorption profiles. To compare the relative peak intensities, the difference between the two absorption spectra L_L and L_T is compared with the RAS spectra and the qualitative agreement is evident [Fig. 2(a), green and red lines].

As the UV-vis spectrophotometer used in this study (Varian Cary-50) records only the specular transmission, the

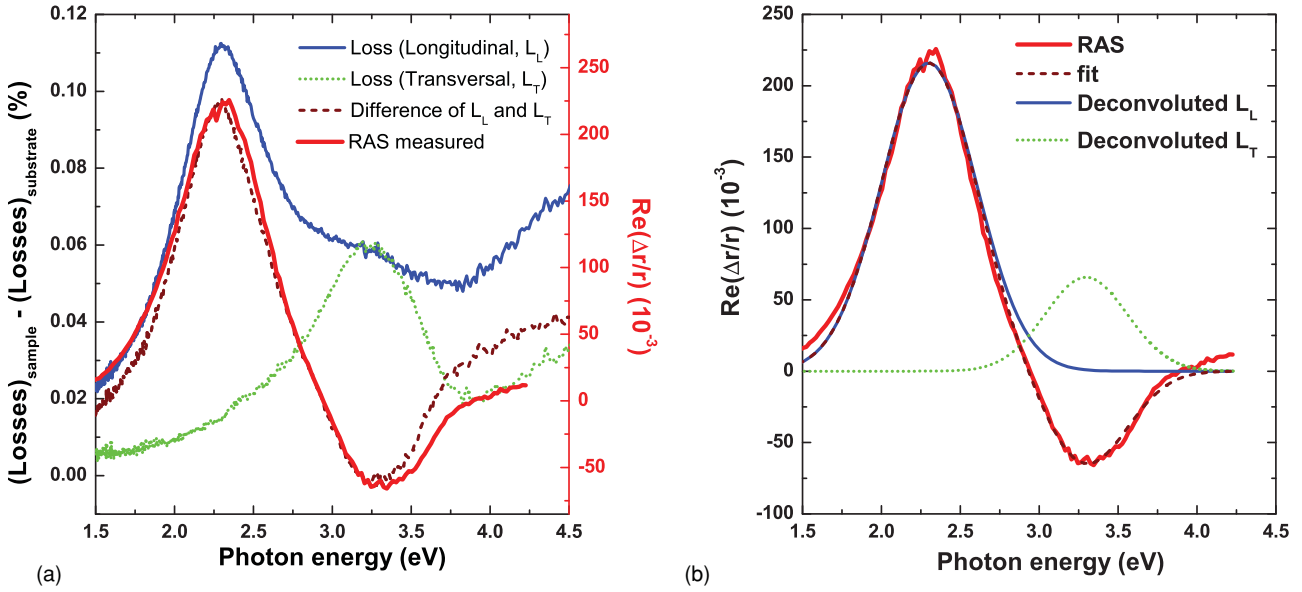

FIG. 2. (Color online) (a) Comparison between *ex situ* RAS and PTS measurements. The absorbance and scattered loss along the step direction (L_L) are shifted with respect to the perpendicular direction (L_T). The spectral shape of the difference between the light losses matches well with the RAS spectra. (b) Fitting of a double Gaussian to the RAS spectrum in order to extract the exact minor peak position.

measured losses are not directly equivalent to an absorption but include reflective and scattered losses. On single-sided polished samples, as used here, this leads to significant light losses caused by Rayleigh scattering at the rough back side of the sample. The data in Fig. 2 have been recorded with respect to a reference sample without Ag islands. At this stage we cannot distinguish between absorption or scattering, as an integrating sphere would be required. However, for comparison of the absorbance and RAS data, this is not a significant problem as both effects can be treated separately. The substrate is fully transparent from 0.45 to 6.5 eV. The apparent UV absorbance in the PTS measurements is simply a Rayleigh-scattering contribution and has its characteristic ω^4 dependence.[32] We stress the point that this is not caused by substrate absorbance, which would complicate the comparison with RAS. The scattering can be caused by possible different losses at the back side of the sample or by enhanced scattering by the Ag islands themselves. This loss is purely added in our simple transmission measurements. The RAS measurements themselves only account for the specular reflected light and hence do not show differences in scattered losses, as the signal is solely generated at the polished front surface.

Even though it is possible to reproduce the RAS features from PTS, the inverse operation is not trivial. RAS measures the difference between the real part of the complex reflection coefficients for light polarized in two orthogonal directions *averaged* on the overall reflection. In order to extract the exact peak position and relative intensities, it is necessary to deconvolute each RA spectrum. This was done by modeling the signal with a double Gaussian, with each peak having a position, amplitude, and width. The deconvolution performed was possible because of substrate transparency. With six free parameters, different choices of the peak positions can reproduce the RAS features. However, by fixing the main peak position using the AbsL PT spectra, a reliable fit was then possible [see Fig. 2(b)] and the secondary peak position, relative peak intensities, and an estimate of the full widths at half maximum could be extracted from the RAS signal.

RAS and the polarization-dependent transmission have been shown to provide similar information, but RAS has the advantage of a greater sensitivity and also allows *in situ* measurements to be performed. Because of these advantages, RAS is the main technique used in the following discussion.

C. Dependency of the optical response on the deposition parameters

The RAS signal observed depends critically on the growth conditions of the Ag NP arrays. A systematic study was undertaken to establish how the RAS changes with substrate morphology, Ag deposition angle, and Ag deposition thickness.

Two samples with off-cut angles of 3° and 6°, respectively, were annealed at 1350 °C for 24 h. AFM inspection confirmed the bunching of steps on the surface. The step-step distance depends on the off-cut and was measured as 137 ± 46 nm for the 3° off-cut sample and 79 ± 22 nm for the 6° off-cut sample. Each sample was scanned in four different areas, and the step-step distance was averaged over at least 150 points. A large-area AFM scan was used to confirm the homogeneity of the surface. The prepared stepped templates were subsequently cut into four smaller pieces, after which they went through a second cleaning procedure and a second AFM study to confirm that the surfaces were unchanged. A piece from each off-cut was then loaded into the vacuum chamber and aligned at a required angle with respect to the deposition direction. RAS spectra were recorded *in situ* during Ag NP array growth. A correction to the deposition time depending on deposition angle was included to ensure that Ag coverage was consistent.

A typical result is shown in Fig. 3. All the RAS spectra show a double-peak feature (Fig. 3, bottom). Figure 3 (top) shows an example of the morphology of a cluster layer determined by

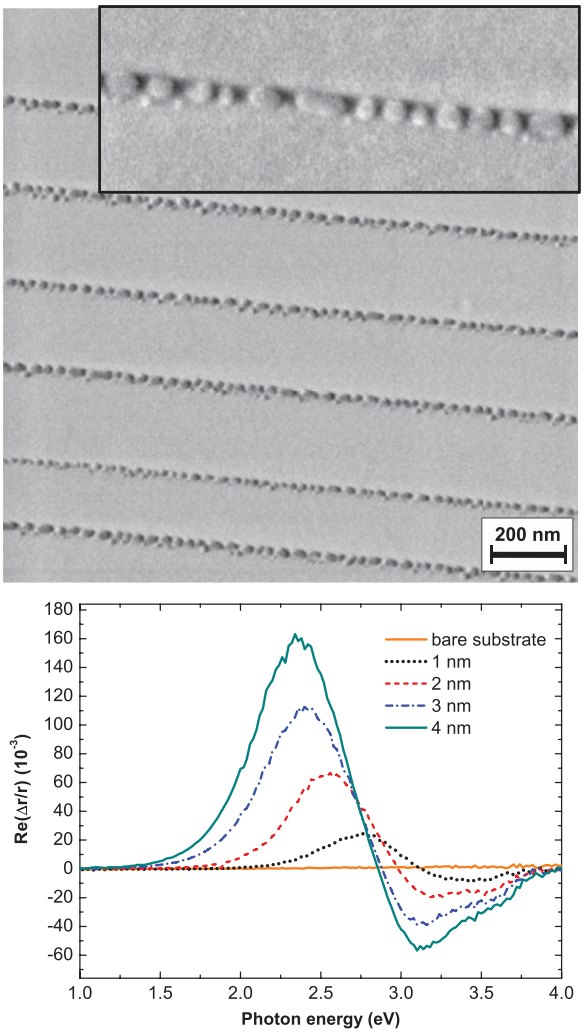

FIG. 3. (Color online) (top) A 1.5×1.5 μm^2 SEM image and magnified (inset) 300×100 nm^2 image of the substrate after 4-nm Ag deposition. The substrate was a 6° miscut sample previously annealed at 1350 °C for 24 h. The sample was loaded in the chamber and inclined at 6° to the Ag atom flux. The surface appears covered by an aligned chain of Ag NPs along the step edge slightly elongated along the chain direction. The measured equivalent radius is 7.9 ± 1.9 nm. (bottom) RAS spectra of the same sample monitored *in situ* for different thicknesses. After deposition, two broad optical resonances are measured, one positive (along the step) and one negative (perpendicular to the step). With increasing deposited thickness, the peak amplitudes increase and the peak positions appear to redshift.

SEM. The surface is covered by aligned chains of NPs having an average radius of 7.9 ± 1.9 nm. NPs are positioned along the outer edge of the steps. This confirms the intuitive view of the growth mechanism, that the adatom flux is directed toward the steps, which act as preferential growth sites. Once the Ag adatoms stick to the surface, they can diffuse along the steps due to the higher surface free energy of the steps. After seed formation, further material deposited results in the growth of the NPs. Using this model a linear increase in the RAS with coverage for both the main and secondary peaks is expected, if the peak profiles do not change significantly.

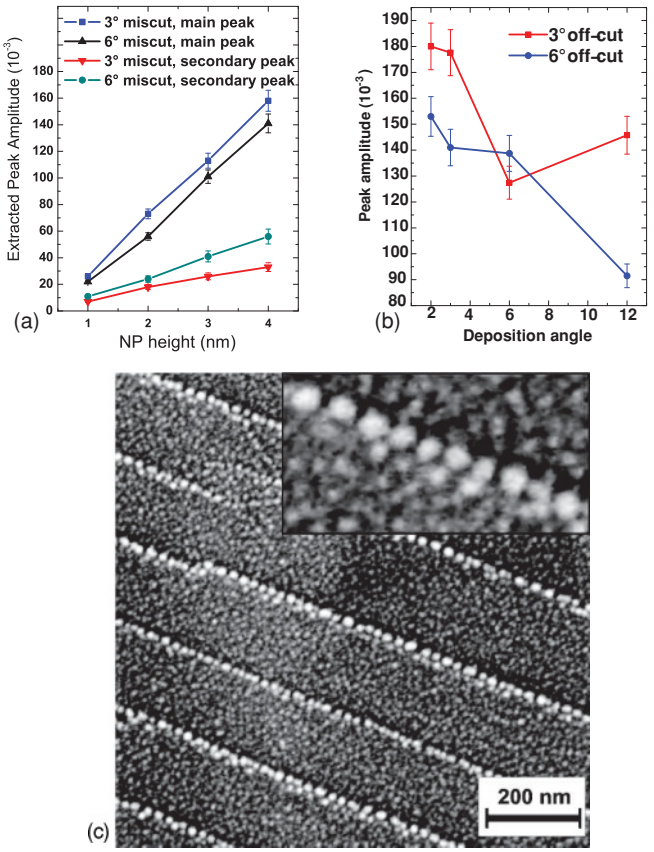

FIG. 4. (Color online)(a) Peak amplitude as a function of the deposited thickness for 6° deposition angle. If the peak width does not increase abruptly (not shown), both the main peak and the secondary peak increase linearly with the amount of Ag on the surface. The behavior is independent of the substrate off-cut. (b) Average main peak height, normalized to 4 nm average height, as a function of deposition angle. (c) SEM image of the 6° miscut, for 4 nm average NP height, at 12° angle of deposition. Significant isotropic deposition on the terrace can be seen, leading to a reduced RAS peak amplitude.

To obtain quantitative information, the curves have been fitted using the two-Gaussian model after fixing the main peak position, and the extracted peak information has been plotted as a function of the nominal NP height for different deposition angles and substrates (see Fig. 4). Both the main and the secondary peak amplitudes increase with the Ag coverage. In particular, all samples that do not show significant increase in the peak width with increasing thickness present a linear increase in the peak amplitudes [Fig. 4(a)], in agreement with the intuitive model. The peak positions depend on the deposition parameters, although the shift in the minor peak is small (Fig. 3). At high deposition angles the redshift of the main peak is proportional to the deposited thickness and the largest peak separation occurs at high coverages.

Figure 4(b) shows that the amplitude generally reduces as the deposition angle increases. This can be understood by reference to the SEM image shown in Fig. 4(c), where for 12° angle of deposition, significant isotropic island formation on the terrace can be seen, which reduces the RAS amplitude. In contrast to the 6° miscut, the 3° miscut shows little change between 6° and 12° angle of deposition. This is consistent

with shadowing effects that are reduced for deposition angles greater than the miscut angle.

IV. THEORY

So far we have shown the dependence of the RAS magnitude and changes in peak positions with coverage and deposition angle. In order to understand this dependence, we need to discuss the measurements within a theoretical framework. There have been numerous discussions on the optical response of LPR[1] and reports of RAS measurements of anisotropic arrangements of metal islands.[30,33–35] However, none of the theoretical models described there can be directly applied to our structures.

From the perspective of the large optical anisotropies ($>50 \times 10^{-3}$), similar RAS amplitudes have been reported for large indium islands on GaAs(001) with a tunable peak position.[33] The response was explained in terms of multipole Mie resonances, as the islands had shape anisotropies and were comparable in size to the wavelength of light. This mechanism cannot be the origin in our case, as the Ag islands are significantly smaller than the wavelength.

Another system where an anisotropic response of Ag islands on an *m*-plane sapphire was reported[30] was explained by the introduction of image charges within the anisotropic substrate. The resulting RAS structures, although similar in shape, are significantly smaller ($<10 \times 10^{-3}$) and appear even with isotropic island distributions. This contrasts to the findings of this work, where a significant morphological anisotropy leads to signals $>100 \times 10^{-3}$ on a negligibly anisotropic substrate plane.

There are other reports of smaller or partly aligned metallic clusters that give rise to optical anisotropies measured by RAS.[34,35] In contrast, the separation between individual nanocluster rows is much greater here, and the measured anisotropy is 1 or 2 orders of magnitude larger. Despite the similar low coverages, the islands are large enough to show metallic behavior, which is not the case for smaller islands of Ag on Si(111) (Ref. 35), and the substrate is not metallic as for Co islands on Au(111). This is a strong indication that the plasmonic effects of metallic NPs in an insulating environment are the physical origin of the measured anisotropy.

The Ag NP arrays were modelled as an infinite one-dimensional (1D) array of equally spaced metallic NPs of radius R, interacting via coupled dipolar plasmon modes. In the quasistatic limit ($R \ll \lambda$), this is the main excitation mode and each nanodot acts as a point antenna. In particular, if the particles are closely spaced, the electric field generated by the mth antenna in direction i produces an electric field in its neighbor's vicinity which is given by[36]

$$\mathbf{E}_{m,i}(t) = \frac{\gamma_i p_{i,m}(t)}{4\pi\varepsilon_0 n^2 d^3}, \tag{2}$$

where ε_0 is the free permittivity, n is the effective refractive index of the medium surrounding the particles, and d is the distance between each dipole. The term γ_i is a polarization-dependent constant, where $\gamma_T = 1$ and $\gamma_L = -2$ for polarization perpendicular and parallel to the dot arrays, corresponding to transverse and longitudinal plasmon modes. If each nanodot is represented as an electric point dipole $p_{i,m} = n_e e x_{i,m}$, where n_e is the number of free electrons displaced by $x_{i,m}$ from the equilibrium position, the equation of motion of the mth oscillator becomes[32]

$$\ddot{p}_{i,m} + \omega_{0,i}^2 p_{i,m} + \Gamma \dot{p}_{i,m} + \sum_{k\neq 0} \gamma_i \omega_{cp,k}^2 (p_{i,m+k} + p_{i,m-k}) = \frac{n_e e^2}{m^*} E_0 e^{i\omega t}. \tag{3}$$

In Eq. (3) the last term represents the incident oscillating electric field, m^* is the optical effective mass, Γ is the electronic relaxation frequency of each NP due to resistive losses in the nanodot, and $\omega_{0,i}$ is the eigenfrequency of the isolated particle. In particular, $\omega_{0,i}$ can be calculated by taking into account shape anisotropy that could lead to splitting of the resonant peak.[2] In the derivation below, an in-plane isotropic NP is assumed and the i index suppressed. The fourth term in Eq. (3) represents the electrodynamic interaction between the dipoles, and it determines the polarization dependence of the optical spectra via a coupling frequency:

$$\omega_{cp,k}^2 = \frac{n_e e^2}{4\pi m^* \varepsilon_0 n^2 (kd)^3}. \tag{4}$$

Assuming periodic boundary conditions and the in-phase oscillations of the long wavelength approximation, it is easily shown that under the assumption of small damping ($\Gamma \ll 1$) and nearest-neighbor interaction, the system behaves like a series of damped harmonic oscillators with an overall effective resonance frequency $\omega_{i,e}^2 = \omega_0^2 + \gamma_i \omega_{cp}^2$, which is polarization dependent. Calculating the difference between the overall effective frequencies for the polarization along ($\omega_{L,e}$) and perpendicular ($\omega_{T,e}$) to the chain and using a Taylor expansion, the following simple formula for the peak separation is derived:

$$\Delta\omega \approx 3\frac{\omega_{cp}^2}{\omega_0}. \tag{5}$$

For higher neighbor interactions, Eq. (3) can be solved exactly with coherent oscillations, obtaining a complex polarization-dependent electric dipole,

$$p_{i,m}(\omega) = \frac{n_e e^2}{m^*}\left(\omega_{i,e}^2 - \omega^2 + i\Gamma\omega\right)^{-1} E_0 e^{i\omega t}, \tag{6}$$

where $\omega_{i,e}^2$ takes into account the interactions up to a cutoff distance. If it is assumed that there are N_l dipole chains per unit area, each containing N_d nanodots, the dielectric function of the nanodot layer is

$$\frac{\varepsilon_i(\omega)}{\varepsilon_0} = 1 + \chi_e = 1 + N_l N_d \frac{n_e e^2}{\varepsilon_0 m^*} p_{i,m}(\omega). \tag{7}$$

Since a positive imaginary part of the dielectric function represents the absorption of energy from the incident electromagnetic wave, a polarization-dependent absorption spectrum whose energy profile is described by Eq. (8) is obtained:

$$\varepsilon_i'' = N_l N_d \frac{n_e e^2}{m^*} \frac{\omega\Gamma}{\left(\omega_{i,e}^2 - \omega^2\right)^2 + \Gamma^2\omega^2}. \tag{8}$$

For comparison with experiment, the Ag NPs were modelled as cylinders having an aspect ratio $R/h = 2$ and a radius $R = 8$ nm. It is assumed that $m^* = 8.7 \times 10^{-31}$ kg (Ref. 37), that the carrier density is 5.85×10^{22} cm^{-3} (Ref. 38),

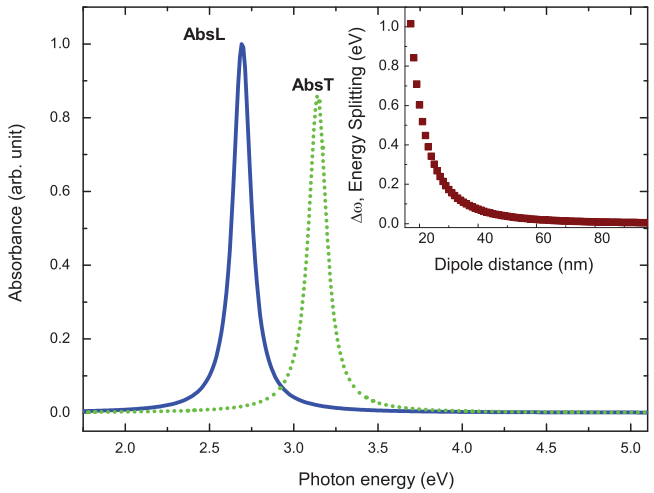

FIG. 5. (Color online) Simulation of the absorption spectra. $R = 8$ nm, $h = 4$ nm, $d = 22$ nm, and $\omega_0 = 2.8$ eV are the parameters used. A clear shift in the two resonances is visible, and the relative magnitude matches qualitatively with the shift measured with transmission spectroscopy(see Fig. 2). The dependence of the energy splitting for polarization along and perpendicular to the NP chain, as a function of the dipole distance, is shown in the inset. When the interdipole distance becomes larger than about 60 nm, the interaction strength becomes negligible, allowing the inter-array interaction to be disregarded.

and the interparticle center-to-center distance is 22 nm. A coupling energy of 0.66 eV is then obtained, indicating a strong interparticle interaction. The magnitude of Γ is determined by the mean free path in the metal NP. If each scattering mechanism is assumed to be independent of the others, the relaxation rate is simply $\Gamma = v_f(1/\lambda_B + C/R)$, where v_f is the fermi velocity, λ_B the bulk mean free path, and C is a constant of the order of unity. For an 8-nm radius Ag NP, with $v_f = 1.38 \times 10^6$ m/s and $\lambda_B = 57$ nm (Ref. 36), the decay rate is $\Gamma \approx 0.8$ eV. Figure 5 shows the absorption spectra for polarization along and perpendicular to the chain. The simulation reproduces the measured PTS qualitatively. In particular, a reasonable energy splitting and a smaller secondary peak amplitude is obtained. The model developed here suggests that for $kd \gg 3R$ the interaction becomes negligible, excluding any strong interarray interaction and the presence of retardation effects.

Using the three-layer model,[39] the RAS features can also be derived from the same microscopic picture. An anisotropic layer of thickness t at the interface between the isotropic bulk alumina dielectric function ε_b and air is assumed. The anisotropic layer consists of an infinite array of dots embedded in an effective refractive index material $n = (1 + n_b)/2$, where the arrays are assumed not to interact. The real part of the RAS is then equal to

$$Re\frac{\Delta r}{r} = \frac{2\omega t}{c} \cdot \frac{\Delta\varepsilon_i''(w)}{\varepsilon_b - 1}. \tag{9}$$

Substituting Eq. (8) into Eq. (9) and using the values previously defined gives a model which shows good agreement with the RAS spectra, given the approximations used.

V. DISCUSSION

The model developed in the previous section provides a useful tool for understanding the RAS features measured during the growth process. The increase in the RAS intensity can be understood simply as an increase in the thickness of Ag and hence, an increase in t in the three-layer model. For high deposition angles the peak shift also increases with the deposited thickness. This behavior is attributed to an increase in the coupling between each oscillator due to the increase in island size: from Eq. (5),

$$\Delta\omega \propto \omega_{cp}^2 \propto n_e. \tag{10}$$

The main limitation of the model is that ω_0 is unknown. However, from the discussion above, it is related to ω_L and ω_T by

$$\omega_0 \doteq \omega_L + 2/3 \times (\Delta\omega). \tag{11}$$

The extracted peak positions show that ω_L decreases and the peak splitting $\Delta\omega$ increases with coverage, indicating that ω_0 is varying slowly and can be treated as a fitting parameter.

The model can be adapted to provide semiquantitative information. Full calculation of the optical response of densely packed anisotropic metallic islands, arranged in ordered arrays on surfaces, remains very difficult due to the combination of anisotropy, interisland electrodynamic interactions, and image charges. It is known, for example, that a departure from in-plane isotropy of isolated Ag islands of as little as 10% can generate significant RAS signals,[30] and SEM shows elongation of the islands along the steps (Fig. 3, inset). A simple calculation of the RAS response of an isolated anisotropic Ag island of similar general dimensions ($R_x = 8$ nm, $R_y = 6$ nm, $h = 4$ nm), embedded in Al_2O_3, shows a doublet structure but with a much-reduced minor peak amplitude. The semiquantitative approach adopted is to allow for anisotropic islands by letting the amplitude of the minor peak vary. From Eq. (8) and Eq. (9),

$$\xi(B,K,V,\Gamma,\omega_0) = B\frac{[\varepsilon_L''(V,\Gamma,\omega_0) - K\varepsilon_T''(V,\Gamma,\omega_0)]}{\varepsilon_b - 1}, \tag{12}$$

where B is the main peak amplitude, K allows the minor peak amplitude to be adjusted, and V is the NP volume for cylindrical islands of aspect ratio 2. The parameter values obtained by using this simple five-parameter fit are given in Table I for the 6° miscut, where shadowing effects are more easily seen. The values of peak height and width, particle volume, and resonance frequency appear quite reasonable, given the approximations of the model. Examples of typical fits are shown in Fig. 6 (top), where both peak shifts and broadening are clearly seen and well reproduced by Eq. (12). The Lorentzian nature of the model results in some excess intensity in the wings of the peaks, as is to be expected if the data are inhomogeneously broadened by dispersion in particle size. However, the Γ parameter can be used as a semiquantitative measure of this broadening. Figure 6 (bottom) shows a strong correlation between the fitted Γ parameter value and the dispersion of the island size, as determined by SEM.

Table I shows that shallow angles of deposition produce a larger dispersion in particle size. This can be explained qualitatively by considering shadowing effects. With increasing

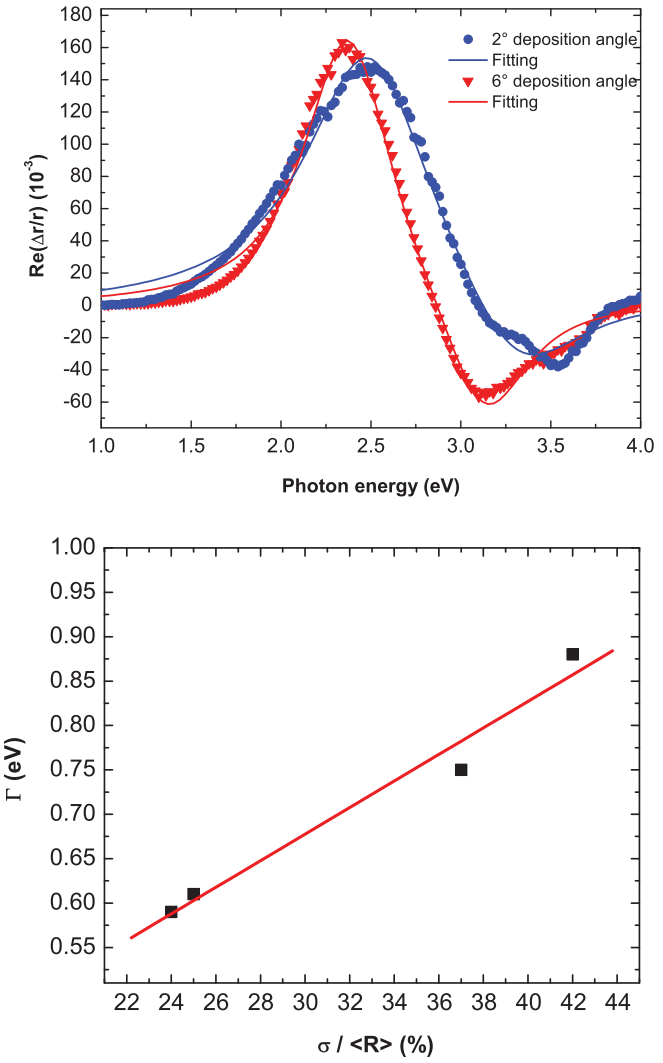

FIG. 6. (Color online) (top) Using Eq. (12), fits of the RAS spectra for the 6° miscut sample, at 2° and 6° deposition angle. (bottom) Plot of fitted Γ value as a function of the percentage dispersion in the island size, determined by SEM, showing the strong correlation.

coverage the height of a NP can increase to a value that, for very shallow angles of deposition, begins to shadow the NP on the adjacent step, which then stops growing. Figure 7(a) shows a schematic of the shadowing effect, and Fig. 7(b) an SEM image for 4 nm coverage and a 2° deposition angle, where arrays of small islands can be seen behind the arrays of larger islands.

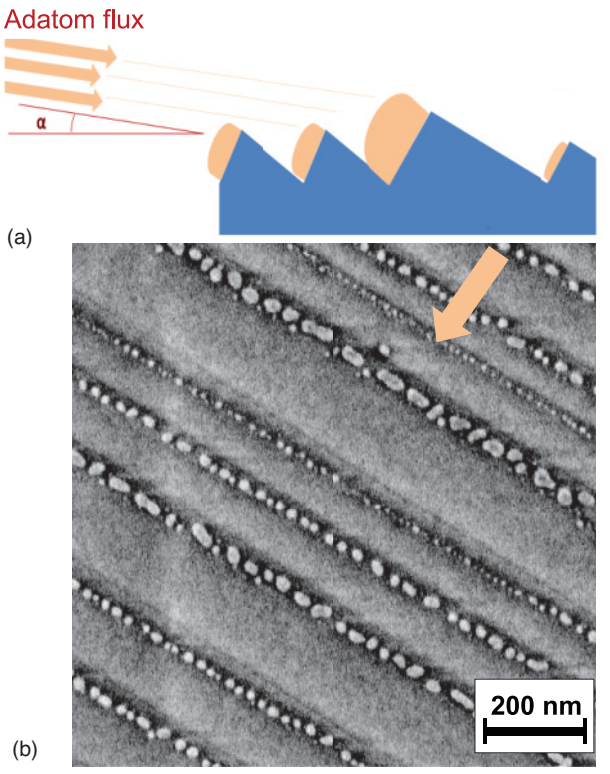

FIG. 7. (Color online) Effects of shadowing on NP array formation for the 6° miscut. (a) Sketch of the shadowing effect. The bigger islands shadow the islands behind, increasing the inhomogeneity in the shape distribution. (b) SEM image for a 2° deposition angle. The arrow indicates flux direction.

The correlation between the fitted Γ value and the dispersion in particle size allows the Γ value, together with the peak amplitude B, to be used as a guide to optimizing growth parameters. Figure 8 shows the fitted Γ value, as a function of deposition angle, for different coverages: similar trends are observed for all coverages. The trend of increased width with coverage indicates that the inhomogeneous dispersion is the dominant contribution to the Γ value, as the larger islands produced at higher coverage will reduce the intrinsic decay rate. It is clear that a more homogeneous distribution of particle size is obtained at higher deposition angles, but the decrease in peak amplitude that accompanies this (Table I) indicates increased growth on the terrace. The optimum conditions are a trade-off between these competing effects, and for this 6° miscut sample, an optimum deposition angle of ≈6° is indicated.

TABLE I. Mean particle radius and interparticle distance for the 6° miscut sample, as determined by SEM, together with fitted parameters using Eq. (12), for different angles of deposition. Errors not shown explicitly are ±0.01.

Deposition angle (°)	R	d	B (10^{-3})	K	V (nm^3)	Γ (eV)	ω_0(eV)
2	6.9 ± 2.9	24 ± 3	372 ± 12	0.51	931 ± 29	0.88	3.10
3	7.9 ± 3	21 ± 5	331 ± 10	0.55	760 ± 21	0.75	3.03
6	7.6 ± 1.9	23 ± 6	259 ± 6	0.63	807 ± 12	0.61	2.92
12	6.6 ± 1.6	21 ± 5	171 ± 5	0.68	690 ± 13	0.60	2.93

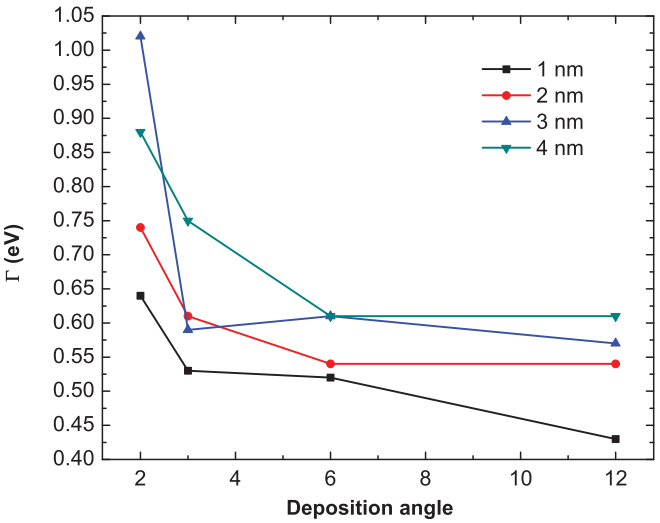

FIG. 8. (Color online) Plot of the fitted Γ value, as a function of deposition angle, for different coverages.

This result shows not only the semiquantitative agreement between a simple model and the RAS measurements, but also offers the possibility of monitoring, *in situ* using RAS, the sample morphology on a macroscopic length scale via the fitted peak width and amplitude.

VI. CONCLUSION

The possibility of growing ordered chains of Ag NP on a step-bunched Al_2O_3 template using glancing-angle deposition has been demonstrated. The samples showed a strong optical anisotropy, which has been measured via polarized transmission spectroscopy and RAS, the equivalence between these two measurement techniques being demonstrated. RAS spectra were measured *in situ* during the growth as a function of the deposited thickness and deposition angle. The RAS signal is attributed to plasmon resonances. In particular, the peak intensity increases linearly with the deposited thickness, and the peak positions are a function of thickness and deposition angle.

A model based on the interaction of point dipoles placed on a 1D infinite array provides a qualitative understanding of the optical behavior of the Ag NP chains. Comparison with SEM results showed that semiquantitative information could be obtained by a simple adaptation of the model to allow for the effect of island anisotropy. The optimum deposition conditions are a trade-off between the competing effects of large island shadowing at small angles and isotropic growth on the terrace at large angles. For a 6° miscut sample at lower coverages, an optimum deposition angle of ≈6° is indicated.

RAS has proved to be a very promising *in situ* growth-monitoring technique, which can provide not only the resonance peak energies and spectral features for anisotropic arrays of plasmonic NPs, but can also be used as a powerful tool for monitoring their order. In particular, information can be provided reproducibly, reliably, and without the need for microscopy techniques, which are time consuming and can require the exposure of the samples to atmospheric contaminants. As the deposition method used is mainly dependent on the geometrical configuration, it can easily be extended to other materials for biosensing purposes or for growth of out-of-plane structures.[40,41]

ACKNOWLEDGMENTS

We would like to thank N. Baadji for the useful suggestions. This work has been funded by the Science Foundation of Ireland, Contract No. 06/IN.1/I91, and conducted under the framework of the INSPIRE programme, funded by the Irish Government's Programme for Research in Third Level Institutions, Cycle 4, National Development Plan 2007-2013. The authors acknowledge use of facilities within the CRANN Advanced Microscopy Laboratory.

*rverre@tcd.ie

[1]U. Kreibig and M. Vollmer, *Optical Properties of Metal Clusters* (Springer, Berlin, 1957).
[2]C. Bohren and D. Huffman, *Absorption and Scattering of Light by Small Particles* (Wiley, New York, 1983).
[3]V. Shalaev and S. Kawata, *Nanophotonics with Surface Plasmons* (Springer, Berlin, 2007).
[4]S. Maier, P. Kik, A. Atwater, and S. Meltzer, Nat. Mater. **2**, 229 (2003).
[5]P. K. Jain, X. Huang, and I. El-Sayed, Plasmonics **2**, 107 (2007).
[6]S. Nie and S. R. Emory, Science **275**, 1102 (1997).
[7]C. Burda, X. Chen, R. Narayanan, and M. A. El-Sayed, Chem. Rev. **105**, 1025 (2005).
[8]A. Sanchez Iglesias, M. Grzelczak, B. Rodrguez-Gonzlez, R. A. lvarez Puebla, L. M. Liz-Marzan, and N. A. Kotov, Langmuir **25**, 11431 (2009).
[9]A. Sugawara, G. Hembree, and M. R. Scheinfein, J. Appl. Phys. **82**, 5662 (1997).
[10]I. V. Shvets, H. C. Wu, V. Usov, F. Cuccureddu, S. K. Arora, and S. Murphy, Appl. Phys. Lett. **92**, 023107 (2008).
[11]P. Ribic and G. Bratina, Surf. Sci. **601**, L25 (2007).
[12]S. Camelio, D. Babonneau, D. Lantiat, L. Simonot, and F. Pailloux, Phys. Rev. B **80**, 155434 (2009).
[13]T. W. H. Oates, A. Keller, S. Noda, and S. Facsko, Appl. Phys. Lett. **93**, 063106 (2008).
[14]E. Fort, C. Ricolleau, and J. Sau-Pueyo, Nano Lett. **3**, 65 (2003).
[15]S. Camelio, D. Babonneau, D. Lantiat, and L. Simonot, Europhys. Lett. **79**, 47002 (2007).
[16]F. Cuccureddu, S. Murphy, I. Shvets, M. Porcu, and H. W. Zandbergen, Nano Lett. **8**, 3248 (2008).
[17]A. Toma, D. Chiappe, D. Massabo, C. Boragno, and F. B. de Mongeot, Appl. Phys. Lett. **93**, 163104 (2008).
[18]C. L. Haynes and R. P. Van Duyne, Nano Lett. **3**, 939 (2003).
[19]Z. Nie, A. Petukhova, and E. Kumacheva, Nat. Nanotech. **5**, 15 (2009).
[20]A. Gademann, I. V. Shvets, and C. Durkan, J. Appl. Phys. **95**, 3988 (2004).

[21] D. E. Aspnes, J. Vac. Sci. Technol. B **3**, 1138 (1985).
[22] P. Weightman, D. S. Martin, R. J. Cole, and T. Farrell, Rep. Prog. Phys. **68**, 1251 (2005).
[23] D. E. Aspnes, J. P. Harbison, A. A. Studna, and L. T. Florez, Phys. Rev. Lett. **59**, 1687 (1987).
[24] J. F. McGilp, Prog. Surf. Sci. **49**, 1 (1995).
[25] Y. Borensztein, W. L. Mochan, J. Tarriba, R. G. Barrera, and A. Tadjeddine, Phys. Rev. Lett. **71**, 2334 (1993).
[26] P. Hofmann, K. C. Rose, V. Fernandez, A. M. Bradshaw, and W. Richter, Phys. Rev. Lett. **75**, 2039 (1995).
[27] J. Heffelfinger and B. Carter, Surf. Sci. **389**, 188 (1997).
[28] L. P. Van, O. Kurnosikov, and J. Cousty, Surf. Sci. **411**, 263 (1998).
[29] F. Cuccureddu, S. Murphy, I. Shvets, M. Porcu, H. Zandbergen, N. Sidorov, and S. Bozhko, Surf. Sci. **604**, 1294 (2010).
[30] J. M. Flores-Camacho, L. D. Sun, N. Saucedo Zeni, G. Weidlinger, M. Hohage, and P. Zeppenfeld, Phys. Rev. B **78**, 075416 (2008).
[31] T. Oates, A. Keller, S. Facsko, and A. Mücklich, Plasmonics **2**, 47 (2007).
[32] J. D. Jackson, *Classical Electrodynamics* (John Wiley, New York, 1992), 3rd ed.
[33] N. Esser, M. Frisch, A. Röseler, S. Schintke, C. Goletti, and B. O. Fimland, Phys. Rev. B **67**, 125306 (2003).
[34] N. Witkowski, Y. Borensztein, G. Baudot, V. Repain, Y. Girard, and S. Rousset, Phys. Rev. B **70**, 085408 (2004).
[35] S. Chandola, J. Jacob, K. Fleischer, P. Vogt, W. Richter, and J. F. McGilp, J. Phys. C **18**, 6979 (2006).
[36] M. L. Brongersma, J. W. Hartman, and H. A. Atwater, Phys. Rev. B **62**, R16356 (2000).
[37] P. B. Johnson and R. W. Christy, Phys. Rev. B **6**, 4370 (1972).
[38] C. Kittel, *Introduction to Solid State Physics* (Wiley, New York, 1986).
[39] J. McIntyre and D. Aspnes, Surf. Sci. **24**, 417 (1971).
[40] X. Wang, C. J. Summers, and Z. L. Wang, Nano Lett. **4**, 423 (2004).
[41] M. Chhowalla, K. B. K. Teo, C. Ducati, N. L. Rupesinghe, G. A. J. Amaratunga, A. C. Ferrari, D. Roy, J. Robertson, and W. I. Milne, J. Appl. Phys. **90**, 5308 (2001).